applied sciences

MDPI

Article

How Useful Are Strain Rates for Estimating the Long-Term Spatial Distribution of Earthquakes?

Sepideh J. Rastin *, David A. Rhoades, Christopher Rollins and Matthew C. Gerstenberger

GNS Science, 1 Fairway Drive, Avalon, P.O. Box 30-368, Lower Hutt 5040, New Zealand; d.rhoades@gns.cri.nz (D.A.R.); c.rollins@gns.cri.nz (C.R.); m.gerstenberger@gns.cri.nz (M.C.G.)
* Correspondence: s.rastin@gns.cri.nz; Tel.: +64-21-2810336

Abstract: Strain rates have been included in multiplicative hybrid modelling of the long-term spatial distribution of earthquakes in New Zealand (NZ) since 2017. Previous modelling has shown a strain rate model to be the most informative input to explain earthquake locations over a fitting period from 1987 to 2006 and a testing period from 2012 to 2015. In the present study, three different shear strain rate models have been included separately as covariates in NZ multiplicative hybrid models, along with other covariates based on known fault locations, their associated slip rates, and proximity to the plate interface. Although the strain rate models differ in their details, there are similarities in their contributions to the performance of hybrid models in terms of information gain per earthquake (IGPE). The inclusion of each strain rate model improves the performance of hybrid models during the previously adopted fitting and testing periods. However, the hybrid models, including strain rates, perform poorly in a reverse testing period from 1951 to 1986. Molchan error diagrams show that the correlations of the strain rate models with earthquake locations are lower over the reverse testing period than from 1987 onwards. Smoothed scatter plots of the strain rate covariates associated with target earthquakes versus time confirm the relatively low correlations before 1987. Moreover, these analyses show that other covariates of the multiplicative models, such as proximity to the plate interface and proximity to mapped faults, were better correlated with earthquake locations prior to 1987. These results suggest that strain rate models based on only a few decades of available geodetic data from a limited network of GNSS stations may not be good indicators of where earthquakes occur over a long time frame.

Keywords: earthquake forecasting; strain rates; multiplicative hybrid models; reverse testing; spatial distribution

check for updates

Citation: Rastin, S.J.; Rhoades, D.A.; Rollins, C.; Gerstenberger, M.C. How Useful Are Strain Rates for Estimating the Long-Term Spatial Distribution of Earthquakes?*Appl. Sci.* **2022**, *12*, 6804. https://doi.org/10.3390/app12136804

Academic Editors: Eleftheria E. Papadimitriou and Alexey Zavyalov

Received: 25 May 2022
Accepted: 2 July 2022
Published: 5 July 2022

Publisher's Note: MDPI stays neutral with regard to jurisdictional claims in published maps and institutional affiliations.

Copyright: © 2022 by the authors. Licensee MDPI, Basel, Switzerland. This article is an open access article distributed under the terms and conditions of the Creative Commons Attribution (CC BY) license (https://creativecommons.org/licenses/by/4.0/).

1. Introduction

Estimation of the long-term spatial distribution of earthquakes is an essential component of Probabilistic Seismic Hazard Analysis (PSHA). In the traditional approach to PSHA, the estimation is based mainly on the combined information from studies of the long-term slip rates and rupture histories of mapped faults and spatial smoothing of the locations of past earthquakes. However, other emerging data streams, including geodetic observations from the global navigation satellite system (GNSS) and derived strain-rate models, seem to offer promise for improving the estimation [1–5]. In a revision of the New Zealand (NZ) National Seismic Hazard Model (NZNSHM) currently being undertaken, we are interested in assessing the relative value of different available data inputs, including information from fault studies, tectonics, the earthquake catalogue, and strain rate models, for estimating the long-term spatial distribution of earthquakes. In particular, we are interested in assessing how strongly strain rate estimates based on a few decades of geodetic data should be weighted when estimating the long-term spatial distribution of earthquakes.

A multiplicative hybrid modelling framework [6] was developed to optimally combine a set of spatially gridded forecasts submitted to the five-year regional earthquake likelihood

models (RELM) experiment in California [7,8]. It was found that, although one best model strongly outperformed all others individually [9], it was possible to find several hybrid models that could outperform the best individual model over the 5-year period of the experiment. Such hybrid models were formed from pairs of models, including the best model as the baseline.

Multiplicative hybrid modelling has since been used to combine gridded information from fault, earthquake, and strain rate covariates in NZ [10,11] with a simple Stationary Uniform Poisson (SUP) baseline earthquake likelihood model. When hybrids only of fault- and earthquake-based variables were considered, any hybrid model that included one particular covariate called "Proximity to Mapped Faults" (PMF) outperformed all hybrids without PMF in both a 20-year fitting period and an independent testing period [10]. The PMF covariate was derived from the locations of NZ mapped faults and their estimated slip rates. Subsequently, Rhoades et al. [11] used models for maximum shear, rotational and dilatational strain rates by Beavan [12], based on GNSS data from 1996–2011, as additional covariates. They found that any hybrid including shear strain rate (BSS) outperformed all hybrids not including BSS in both the 20-year fitting period and an independent testing period.

In the present study, we restrict our attention to (maximum) shear strain rate models. In addition to BSS, we consider the global shear strain rate model of Kreemer et al. [13] based on GNSS data over the period 1996–2013 (GSS) and an updated NZ strain rate model by Haines and Wallace [14] based on GNSS data from 1995–2013 (HWS). We analyse the performance of multiplicative hybrids during the fitting and testing periods used by Rhoades et al. [11] with GSS and HWS as alternative strain rate covariates. We then examine the stability of the multiplicative modelling results by testing them against earthquakes from 1951 to 1986. Furthermore, we evaluate the strain rate and other covariates as earthquake predictors using Molchan error diagrams. We also produce smoothed scatter plots of covariate values corresponding to targeted earthquakes against time from 1951 to 2020. These results are relevant to the question of how useful strain rate estimates are for the assessment of long-term seismic hazards.

2. Method and Data

2.1. Multiplicative Hybrid Model

We follow the method used by Rhoades et al. in [6,10,11] to produce hybrid earthquake likelihood models from a baseline model and a set of covariates. As in [10,11], the stationary uniform Poisson (SUP) model is used as the baseline model, and subsets of the available spatially varying covariates are assimilated into it to form a range of hybrid models.

The hybrid and baseline models are regional earthquake likelihood models [8] defined by a set of expected numbers of earthquakes $\{\lambda(j,k)\}$ in cells of location, indexed by j, and magnitude, indexed by k, where $j = 1, \ldots, n_j$, and $k = 1, \ldots, n_k$. The baseline model is denoted by $\{\lambda_0(j,k)\}$, and the hybrid model by $\{\lambda_H(j,k)\}$. The n_i covariates take values in the location cells only and are denoted by $\{\rho_i(j), j = 1, \ldots, n_j; i = 1, \ldots, n_i\}$. The covariates may be real-valued or categorical (e.g., binary) variables. The multiplicative hybrid model is of the form

$$\lambda_H(j,k) = \lambda_0(j,k) \exp(a) \Pi_{i=1}^{n_i} f_i[\rho_i(j)]. \quad (1)$$

Here, a is a normalising parameter that ensures the total expected numbers of earthquakes in the hybrid model match with the actual number in the catalogue to which it is fitted. The function f_i converts a cell value of the ith covariate into a multiplier to be applied to the corresponding cells of the baseline model. For a real-valued covariate, the multiplier f_i is a non-negative, monotone, non-decreasing and nonlinear function of the form

$$f_i[\rho] = \exp(b_i[\ln(1+\rho)]^{c_i}), \ (b_i \geq 0; c_i \geq 0). \quad (2)$$

It thus preserves the ordering of values in cells but not the ratio of values between cells. For a binary covariate, where $\rho(j)$ takes only the values 0 and 1, f_i is of the form

$$f_i[\rho] = \exp(d_i \rho), \tag{3}$$

where adjustable parameters d_i are allowed to take positive or negative values.

The adjustable parameters in the hybrid model are the normalising parameter a, the shape parameters b_i and c_i for each real-valued covariate, and d_i for each binary covariate. In fitting a hybrid, the parameters are chosen to optimize the log-likelihood, ln L, of the target earthquakes, given by Rhoades et al. [15] as

$$\ln L = \sum_{n=1}^{N} \ln \lambda_H(j_n, k_n) - \hat{N}_H, \tag{4}$$

in which the target earthquakes occur in cells $\{(j_n, k_n), n = 1, \cdots, N\}$, and $\hat{N}_H$ denotes the total expected number of target earthquakes, i.e.,

$$\hat{N}_H = \Sigma_{j=1}^{n_j} \Sigma_{k=1}^{n_k} \lambda_H(j, k). \tag{5}$$

Following Rhoades et al. [6], the corrected information gain per earthquake (IGPEc) of a fitted hybrid model $\{\lambda_H(j,k)\}$ over the baseline model $\{\lambda_0(j,k)\}$ is calculated using

$$\text{IGPEc} = \frac{-\Delta}{2N}, \tag{6}$$

in which Δ is the change in the corrected Akaike Information Criterion (AICc) between the hybrid model and the baseline model. AICc is defined by

$$\text{AICc} = -2 \ln L + 2p + \frac{p+1}{N-p-1}, \tag{7}$$

in which p is the number of fitted parameters in the hybrid model, and N is the number of target earthquakes [16].

Confidence limits on IGPEc are estimated using an adaptation of the T-test [15] for comparing one earthquake likelihood model to another based on independent data, as described by Rhoades et al. [6].

For testing of the fitted models on independent data, in which there are no adjustable parameters, the information gain per earthquake (IGPE) is simply the change in log-likelihood between the hybrid and baseline models divided by the number of target earthquakes, and the T-test given in [15] applies.

The covariates are defined on the NZ Collaboratory for the Study of Earthquake Predictability (CSEP) testing grid of 0.1-degree rectangular cells [17]. The covariates used in this study are strain rates (BSS, GSS, and HWS), Proximity to the Plate Interface (PPI), Proximity to Mapped Faults (PMF), and Fault in cell (FLT). We have provided details of strain rate covariates in Appendix A. The non-strain-rate covariates are slightly modified compared to those used by Rhoades et al. [10]. We have provided information on these modifications in Appendix B. It is not meant to include the smoothed seismicity covariates from Rhoades et al. [10] because they were fitted to the earthquakes prior to 1986 that are now used for reverse testing. Figure 1 displays the spatial distributions of the non-strain-rate covariates.

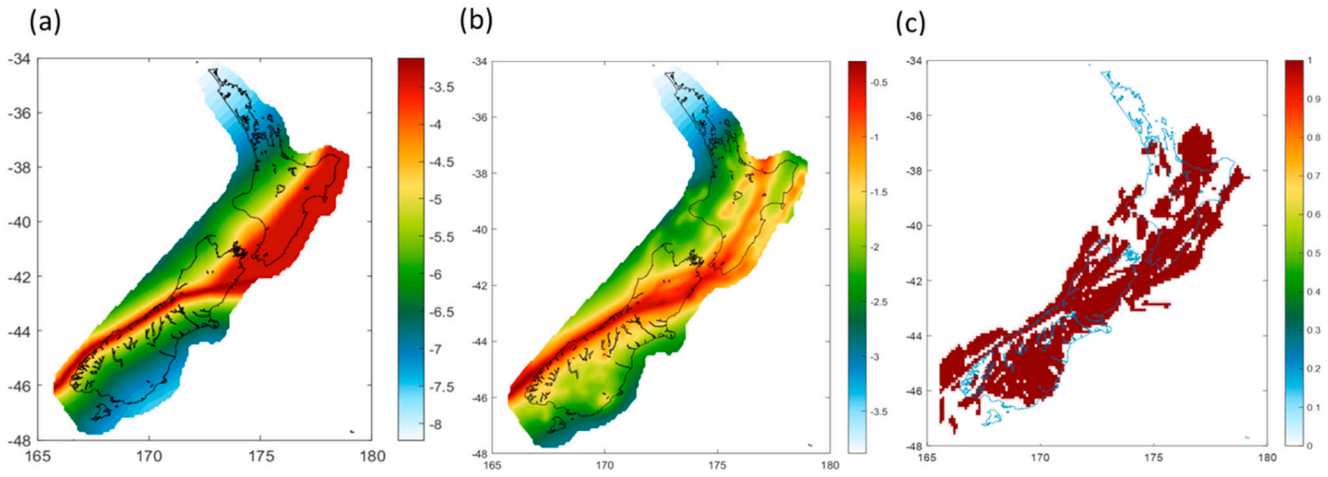


Figure 1. Spatial distributions of the modified (**a**) Proximity to plate interface (PPI) and (**b**) Proximity to mapped faults (PMF) covariates (log of grid cell values). The colour scale shows the logarithm of the relative rate. (**c**) Spatial distribution of updated Fault in cell (FLT) binary covariate using all faults from the New Zealand Community Fault Model [18].

The strain rate covariates (BSS, GSS, and HWS) are included separately in hybrid models as single covariates and with all possible combinations of the other (non-strain-rate) covariates. Hybrid models are fitted to the period 1987–2006, with forward testing over the period 2012–2015 and reverse testing over the period 1951–1986. The spatial distributions of the strain rate covariates are shown in Figure 2.

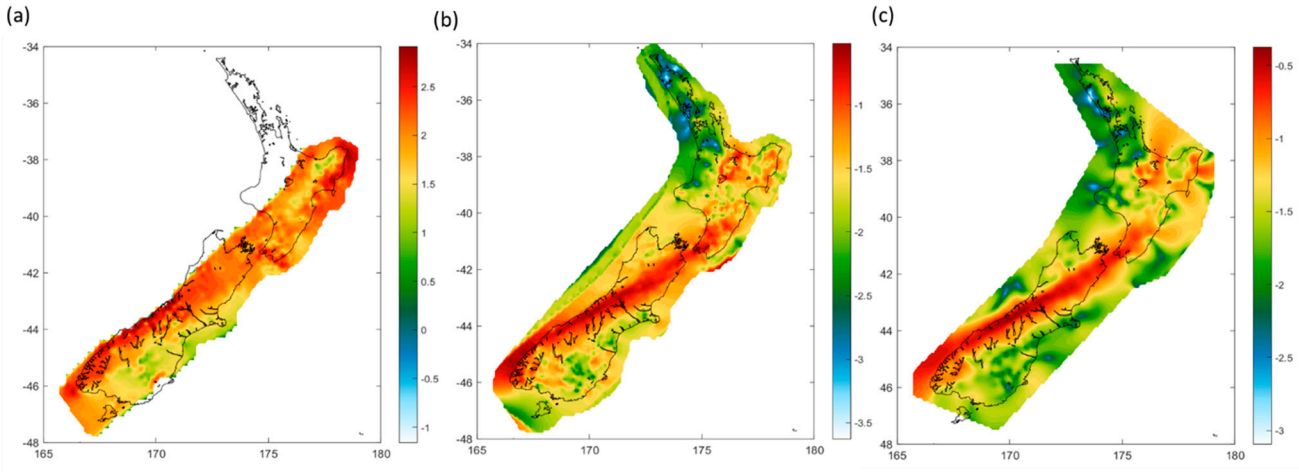


Figure 2. Spatial distribution of (**a**) GSS (1996–2013), (**b**) BSS (1996–2011), and (**c**) HWS (1995–2013) strain rate models in the New Zealand CSEP testing region. The colour scale shows the logarithm of the relative rate.

2.2. Molchan Error Diagram

We obtain Molchan error diagrams [19,20] for all covariates at different time intervals. Molchan error diagrams are equivalent to Receiver Operating Characteristic curves, which have been widely used in other contexts [21,22]. They can be used to investigate the correlation between a spatially distributed covariate and the spatial distribution of target earthquakes.

The error diagram is based on the concept of an alarm being declared wherever a covariate exceeds a certain threshold. As the threshold is decreased, the proportion of space occupied by alarms increases, and the proportion of target earthquakes outside of the alarm space (i.e., the proportion of "unpredicted earthquakes") decreases. In the error diagram, the proportion of unpredicted earthquakes is plotted against the proportion of

space occupied by alarms, but the threshold for declaring an alarm is not shown. The error diagram is, therefore, a monotone decreasing curve.

For an ideal predictor, all target earthquakes are predicted by an alarm occupying almost zero area. The error diagram curve then consists of the line segments joining the point (0,1) to (0,0) and the point (0,0) to (1,0). For a totally uninformative predictor, the proportion of space occupied would be the same as the proportion of predicted earthquakes. The error diagram curve would then be the diagonal line joining (1,0) to (0,1).

The area above the error diagram curve within the unit box is called the Area Skill Score (ASS) [23]. The ASS is a rough measure of the overall potential the covariate has for predicting the locations of target earthquakes. An ideal predictor has an ASS of 1, and a totally uninformative predictor has an ASS of 0.5.

If a covariate is better correlated with the locations of target earthquakes during one time period than another, then the error diagram will vary with time accordingly. Therefore, we plot and compare error diagrams for different periods.

2.3. Scatter Plot of Covariates for the Target Earthquakes

We have investigated gradual changes over time in the correlation of a covariate with earthquake locations using a simple scatter plot. The scatter plot displays values of a covariate in cells corresponding to target earthquakes versus time. Trends in these values, whether decreasing or increasing, are revealed by a smoothed local regression fit to the data.

2.4. Data

The target earthquakes in this study are events from 1951 to 2020 with a hypocentral depth between 0 and 40 km and a magnitude greater than 4.95 (GeoNet preferred magnitude) within the CSEP testing region [17]. The events of interest were extracted from the GeoNet catalogue of NZ earthquakes (www.geonet.org.nz; last accessed on 1 July 2022). Magnitudes assigned by GeoNet are mostly local magnitudes, but moment magnitudes are preferred for larger events. The catalogue is consistent with that used by Rhoades et al. [10,11] within the fitting and testing periods of those studies.

3. Results

3.1. Hybrid Models

IGPE estimates and 95% confidence intervals of the hybrid models with BSS for the fitting period (1987–2006), forward testing period (2012–2015), and reverse testing period (1951–1986) are presented in Figure 3. Corresponding results with GSS and HWS are presented in Figures 4 and 5, respectively. The IGPEs are relative to the SUP baseline model. To compare the IGPEs of two hybrid models, one needs to obtain the differences between their log-likelihoods for the target earthquakes and perform a T-test on those differences. In this study, we have only presented T-tests for comparing each hybrid model to the baseline model.

The combination of covariates contributing to each hybrid is indicated by a model number composite. This composite combines the baseline model identifier with those of the selected covariates: “1” for SUP, “2” for PPI, “3” for PMF, “4” for FLT, and “5” for strain rate covariate (BSS, GSS, or HWS). Table 1 contains the name, acronym, and identifier for the baseline model and covariates. For example, the composite “123” represents a hybrid with SUP as baseline and PPI and PMF as covariates.

Table 1. Name, acronym, and identifier for the baseline model and covariates.

Covariate or Model Name	Acronym	Identifier
Stationary uniform Poisson baseline model	SUP	"1"
Proximity to plate interface covariate	PPI	"2"
Proximity to mapped faults covariate	PMF	"3"
Fault in cell covariate (binary)	FLT	"4"
Beavan shear strain rate covariate	BSS	"5"
Global shear strain rate covariate	GSS	"5"
Haines and Wallace shear strain rate covariate	HWS	"5"

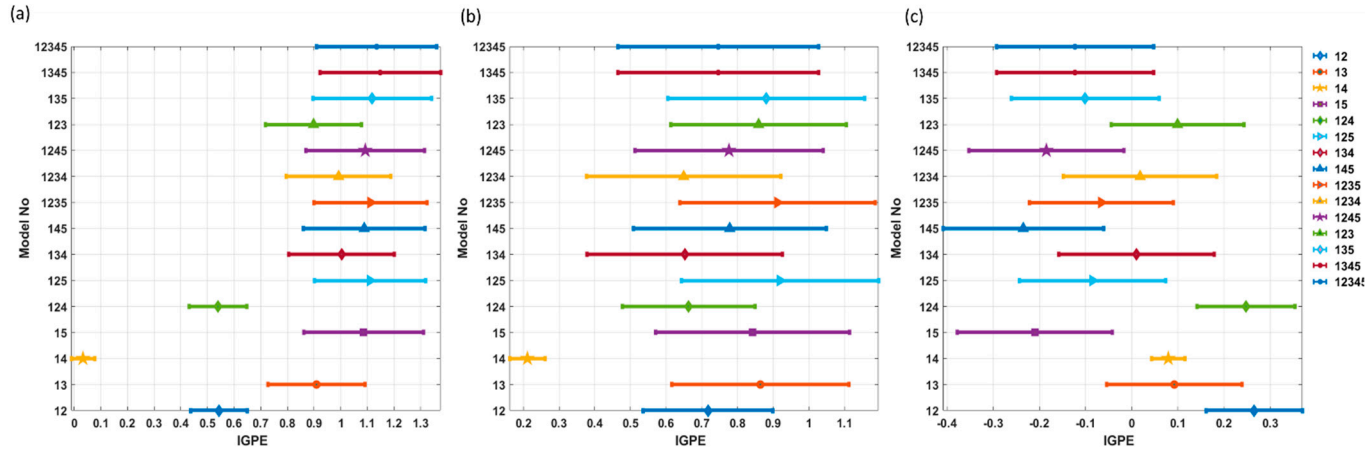


Figure 3. Information gain per earthquake (IGPE) of hybrid models relative to SUP baseline model with the Beavan shear strain rate (BSS) covariate. The combination of covariates contributing to each hybrid is indicated by the model number, which is a composite of the numbers corresponding to the baseline model and selected covariates, as follows: 1-SUP; 2-PPI; 3-PMF; 4-FLT; 5-BSS. (**a**) Fitting period (1987–2006); (**b**) Forward testing period (2012–2015); (**c**) Reverse testing period (1951–1986). Error bars are 95% confidence intervals.

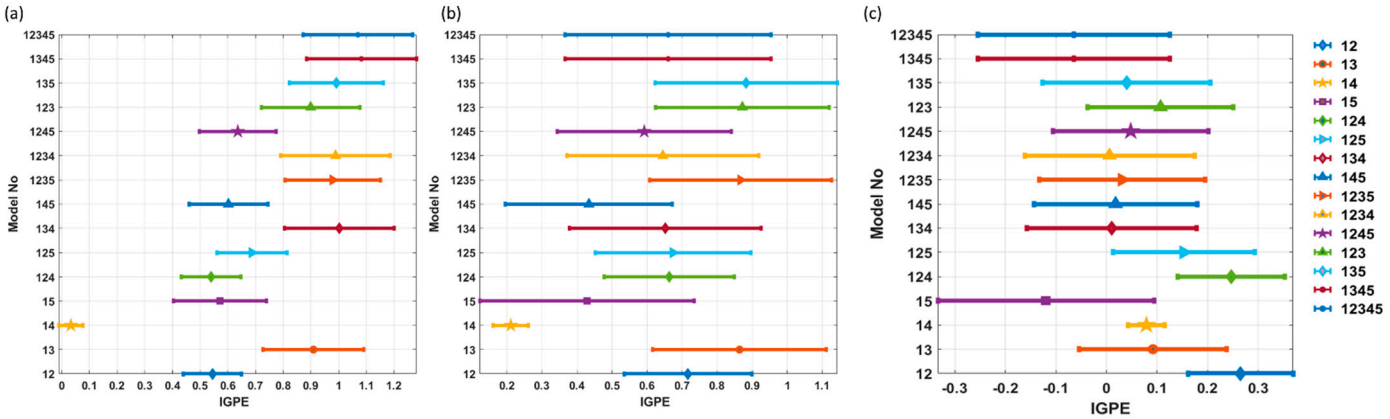


Figure 4. Information gain per earthquake (IGPE) of hybrid models relative to SUP baseline model with the GSS strain rate covariate. The combination of covariates contributing to each hybrid is indicated by the model number, which is a composite of the numbers corresponding to the baseline model and selected covariates, as follows: 1-SUP; 2-PPI; 3-PMF; 4-FLT; 5-GSS. (**a**) Fitting period (1987–2006); (**b**) Forward testing period (2012–2015); (**c**) Reverse testing period (1951–1986). Error bars are 95% confidence intervals.

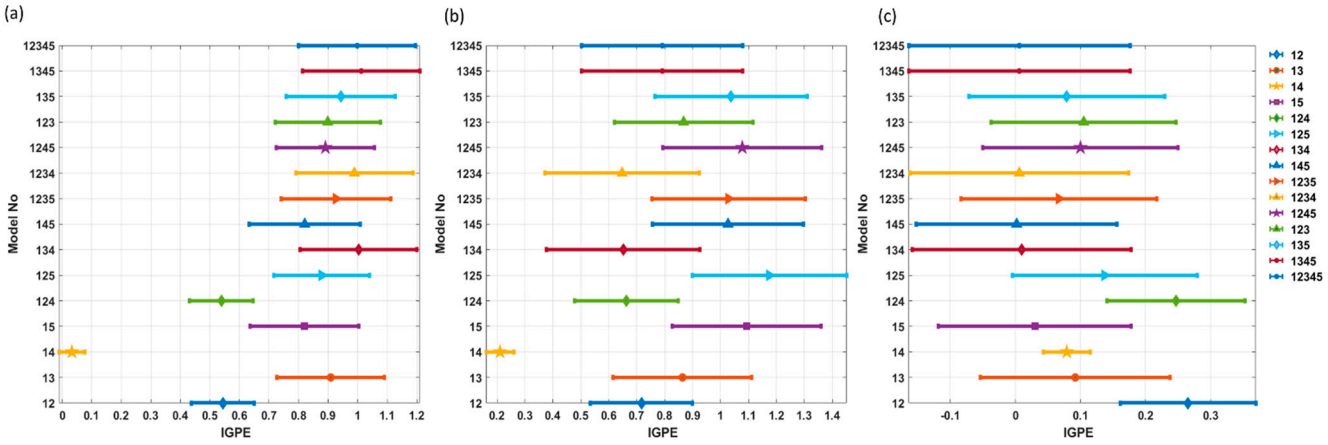


Figure 5. Information gain per earthquake of hybrid models relative to SUP baseline model with the HWS strain rate covariate. The combination of covariates contributing to each hybrid is indicated by the model number, which is a composite of the numbers corresponding to the baseline model and selected covariates, as follows: 1-SUP; 2-PPI; 3-PMF; 4-FLT; 5-HWS. (**a**) Fitting period (1987–2006); (**b**) Forward testing period (2012–2015); (**c**) Reverse testing period (1951–1986). Error bars are 95% confidence intervals.

Results for the fitting and forward testing period with the BSS covariate were previously reported by Rhoades et al. [11] and showed that the IGPE was higher for all hybrid models including BSS than for all models not including BSS. Here, with modified non-strain-rate covariates for the fitting period (Figure 3a), all hybrids including BSS (composites containing "5") have IGPE > 1.1. The largest IGPE is 1.48 for "1345". On the other hand, all hybrids excluding BSS have IGPE < 1.1. For these, the largest IGPE is 1.00 for "134".

When the BSS covariate is replaced by either GSS (Figure 4a) or HWS (Figure 5a), the results for the fitting period are different. With BSS, "15" (SUP + BSS) has the largest IGPE amongst all the simple hybrids. However, with GSS and HWS, "13" (SUP + PMF) outperforms "15". However, similar to BSS, the largest IGPE values for GSS and HWS are obtained for "1345" (1.08 and 1.01, respectively).

For the forward testing period, the hybrids again perform differently with different strain rate covariates. With BSS (Figure 3b), the hybrids including strain rates are not as dominant as in Rhoades et al. [11], due to the revision of the non-strain-rate covariates (Appendix B). Hybrid "13" performs almost as well as "15", i.e., the IGPEs of both hybrids are similar. With GSS (Figure 4b), "13" performs much better than "15". With HWS, "15" outperforms "13" and all other simple hybrids. Moreover, all hybrid models including HWS outperform most hybrids without HWS except "123".

Hybrids with HWS perform not quite as well as those with BSS in the fitting period (Figures 4a and 5a) but better than those with BSS in the forward testing period (Figures 4b and 5b). Larger IGPEs in the forward testing period may be due to a partial overlap between this period (2012–2015) and the time range of GNSS data used to derive HWS (1995–2013). Hybrids with GSS perform not as well in either the fitting or forward testing period as their counterparts with BSS and HWS (Figure 4a, Figure 5a, and Figure 6a, and Figure 4b, Figure 5b, and Figure 6b, respectively).

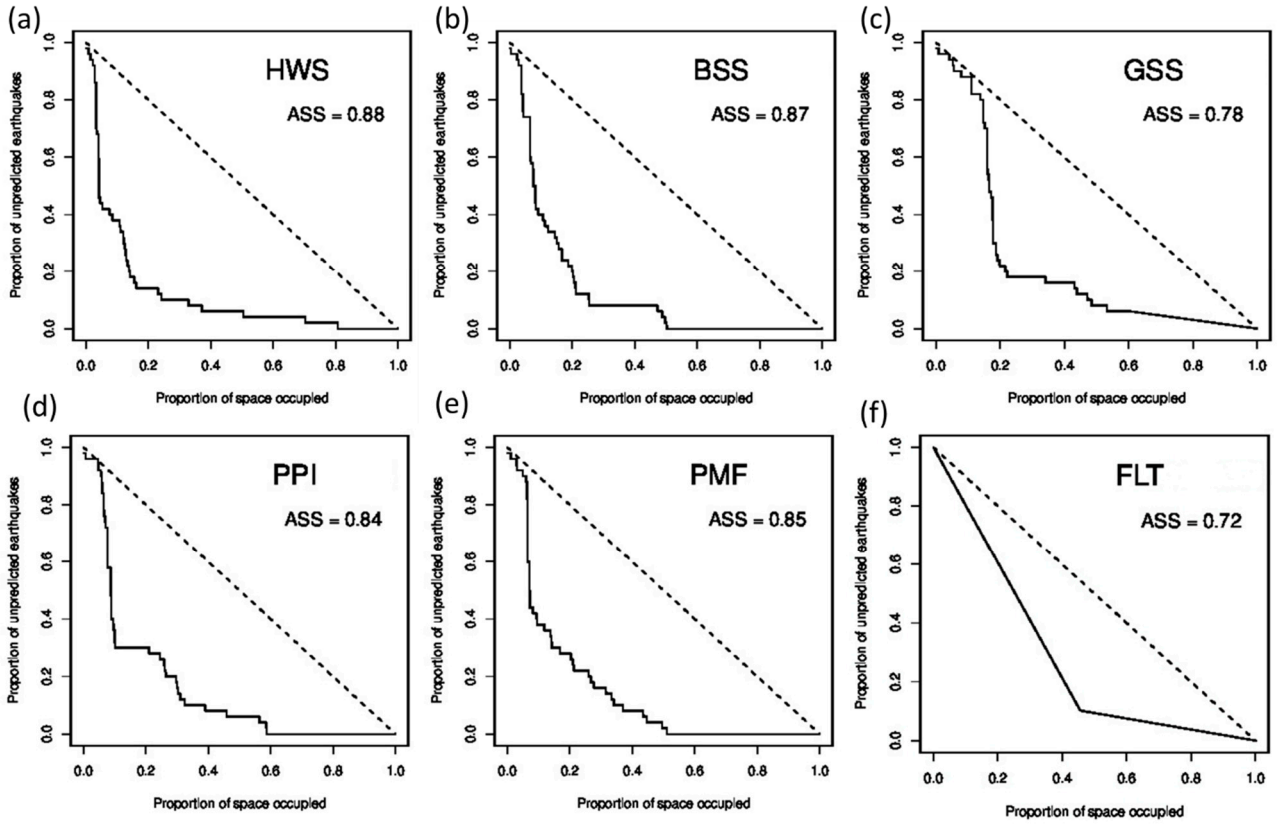


Figure 6. Molchan error diagrams for covariates (**a**) HWS, (**b**) BSS, (**c**) GSS, (**d**) PPI, (**e**) PMF, and (**f**) FLT, and target earthquakes in the forward test period 2012–2015.

Hybrids with BSS perform poorly in the reverse testing period 1951–1986 (Figure 3c) and even worse than those without BSS, including the SUP baseline (since their IGPEs are negative). For all models without BSS, IGPE is mostly lower than in the fitting and forward testing periods. The largest IGPE for the reverse testing period was 0.27, obtained by hybrid "12", and is only half of the corresponding IGPE for the fitting period.

With GSS, the IGPE of the "15" hybrid is again negative in the reverse testing period, as are the IGPEs for "12345" and "1345". With HWS, the "15" hybrid has a small positive IGPE of 0.03 for the reverse testing period, and all the hybrids have small positive IGPE values (Figure 5c). Thus, hybrid models with HWS perform slightly better than the corresponding models with BSS or GSS in the reverse testing period (c.f. Figures 3c, 4c and 5c). However, overall, the performance of hybrids including strain rates is poor in the reverse testing period.

3.2. Error Diagrams

A hybrid model can perform poorly in an independent testing period either because the covariates that contribute to it are not well correlated with earthquake locations or because the model is overfitted to a training period in which the covariates are better correlated with earthquake locations than in the testing period. Molchan error diagrams give an indication of the correlation between covariates and earthquake locations in different time periods independent of any model fitting. For the error diagram analysis, we have split the 36-year reverse testing period into three separate 12-year periods.

In the forward testing period 2012–2015, the non-strain-rate covariates PPI and PMF and strain covariates BSS and HWS are well-correlated with the locations of target earthquakes, as shown by the error diagrams deviating far below the diagonal (Figure 6). The ASS for each of these covariates is rather high, between 0.85 and 0.88. HWS has the highest ASS of 0.88. Again, this may be due to the partial overlap between the forward testing

period and the time range of GNSS data used to derive HWS. In contrast, GSS and FLT have smaller ASS values of 0.78 and 0.72, respectively, which implies they are not as strongly correlated with the locations of target earthquakes. This is reflected in the error diagrams not reaching as far below the diagonal as those of the other covariates.

The correlation between the covariates and target earthquake locations varies appreciably over time (Figure 7). The strain rate covariates, especially BSS, show this variation more than the other covariates. Figure 7 compares error diagrams and ASS values for each covariate in five selected time periods—1951–1962; 1963–1974; 1975–1986; 1987–2006; and 2012–2015.

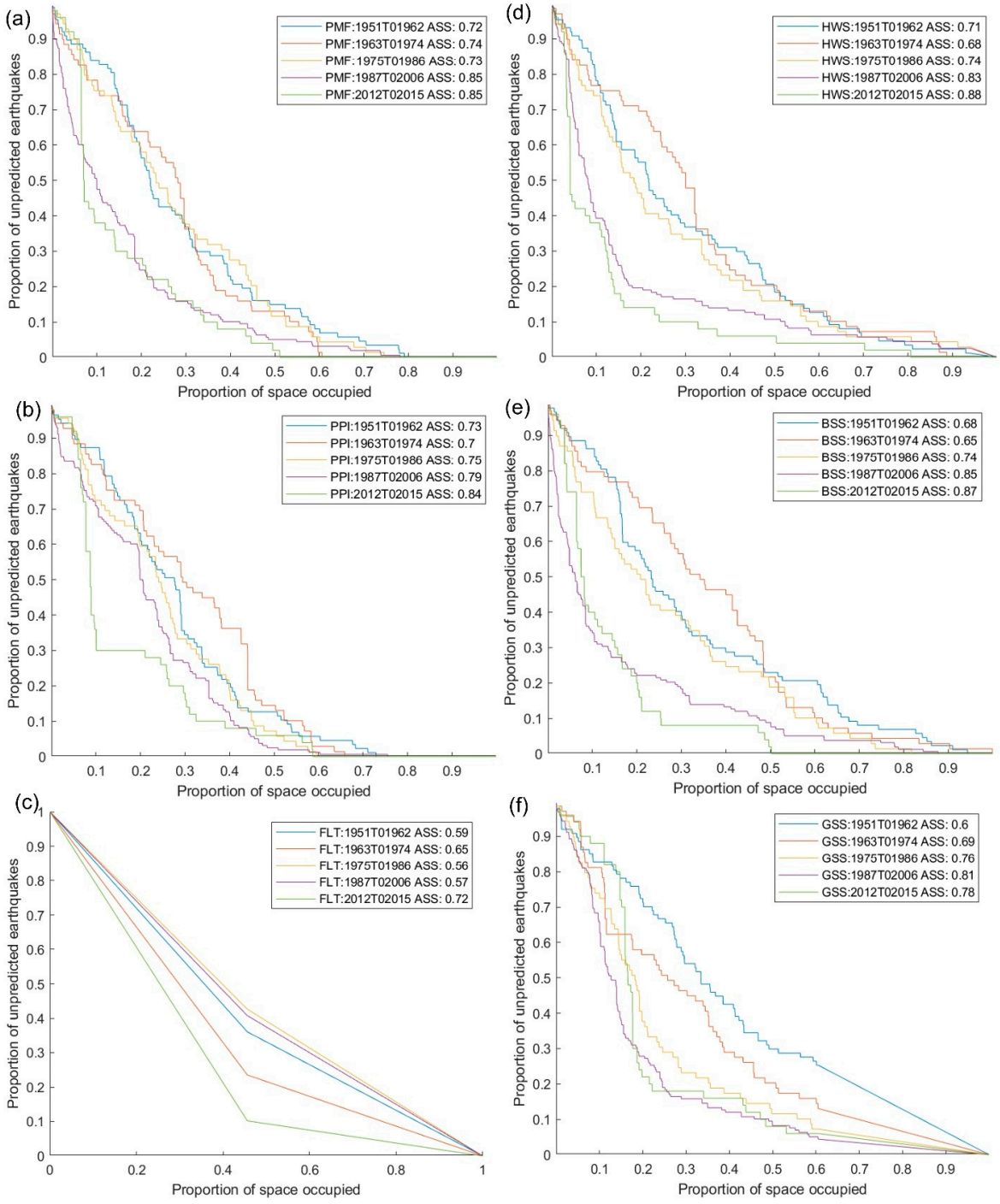


Figure 7. Molchan error diagrams for the covariates during different time intervals. (**a**) HWS; (**b**) PMF; (**c**) BSS; (**d**) PPI; (**e**) GSS; (**f**) FLT.

The range of variations in ASS values for a single covariate is an indicator of how widely the correlation varies between time periods. For the PMF covariate (Figure 7a), the correlation is equally high during fitting and forward testing periods ($ASS_{1987–2006} = ASS_{2012–2015} = 0.85$) and lowest during 1951–1962 ($ASS_{1951–1962} = 0.72$). For the PPI covariate (Figure 7b), the correlation with earthquake locations is highest during 2012–2015 ($ASS_{2012–2015} = 0.84$) and lowest during 1963–1974 ($ASS_{1963–1974} = 0.70$). For the FLT covariate (Figure 7c), the correlation is highest during the forward testing period ($ASS_{2012–2015} = 0.72$) and lowest during 1975–2006 ($ASS_{1975–1986} = 0.56$, $ASS_{1987–2006} = 0.57$). For the HWS covariate (Figure 7d), the correlation is highest during 2012–2015 ($ASS_{2012–2015} = 0.88$) and lowest during 1963–1974 ($ASS_{1963–1974} = 0.68$). For the BSS covariate (Figure 7e), the correlation is highest during 2012–2015 ($ASS_{1987–2006} = 0.87$) and lowest during 1963–1974 ($ASS_{1963–1974} = 0.65$). For the GSS covariate (Figure 7f), the correlation is highest during 1987–2006 ($ASS_{1987–2006} = 0.81$) and lowest during 1951–1962 ($ASS_{1951–1962} = 0.60$). The low ASS can be explained by the fact that many of the target events in 1951–1962 were located where GSS had a value of zero (Figure 8).

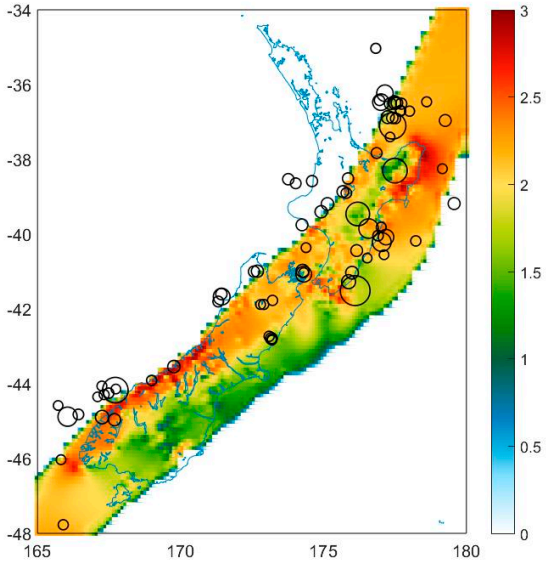


Figure 8. Spatial distribution of GSS and target earthquakes during 1951–1962.

The variation of ASS values with time period is plotted for each covariate in Figure 9. No covariate has a consistently higher ASS than the other covariates across all time periods. As can be seen, the highest ASS among the covariates in 1951–1962 is that of PPI, in 1963–1974 that of PMF, in 1975–1986 that of GSS, in 1987–2006 that of BSS, and in 2012–2015 that of HWS. At the other end of the scale, the FLT covariate has the lowest ASS value in all time periods except 1963–1974, in which it shares the lowest value with BSS. Among the strain rate covariates, the highest ASS value is that of the HWS from 1951 to 1962 and 2012 to 2015, GSS from 1963 to 1974 and 1975 to 1986, and BSS from 1987 to 2006. Figure 9 also shows that the HWS covariate has a higher ASS value than BSS in all time periods except 1987–2006—the fitting period for the multiplicative models.

3.3. Smoothed Scatter Plots

To give a better insight into changes over time in the correlation of covariates with earthquake locations, we plotted the covariate values for the cells corresponding to target earthquakes versus time over the period 1951–2020. We then fitted a trend curve using locally weighted scatter plot smoothing (lowess) based on Cleveland's method in [24]. We observed clear trends in the strain rate covariate values corresponding to target earthquake locations over the period 1951–2020, as shown by Figure 10.

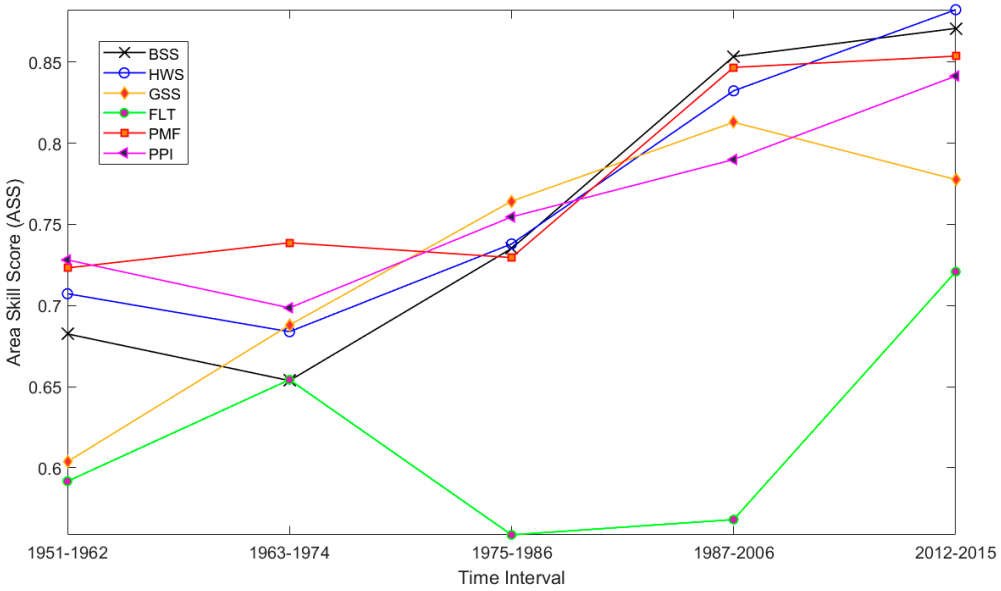


Figure 9. Area Skill Score (ASS) of Molchan error diagram for covariates over different times.

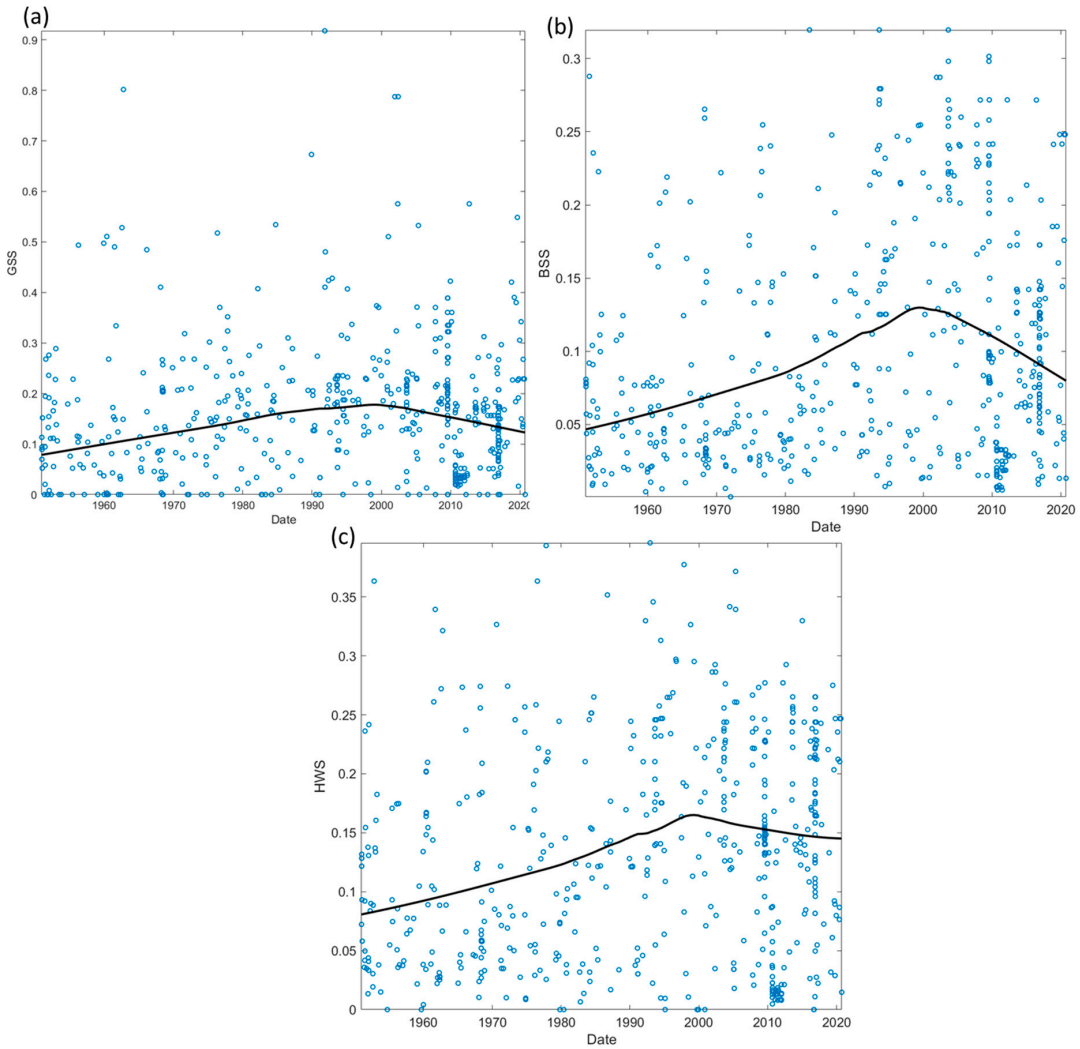


Figure 10. Smoothed scatter plots of (**a**) GSS, (**b**) BSS, and (**c**) HWS strain rate covariates for targeted earthquakes against time from 1951 to 2020.

The trend is stronger for BSS and HWS than for GSS. However, for all three covariates, the smoothed trend line starts from its lowest level in 1951, rises gradually to a peak in 1999, and then tails off somewhat through to 2020. However, the HWS curve also tails off less than the others. These results confirm and elaborate on the trends over time that was observed in Figures 8 and 10. The HWS model was extracted from the longest period of recordings (1995–2013) and a larger number of GNSS stations compared with the GSS and BSS models. In addition, unlike BSS and GSS that were both based on an older method of Haines and Holt [25–27], the HWS model was derived using the novel VDOHS technique [14]. Such differences could explain the differences observed in the smoothed scatter plots versus time.

We observed that FLT was the only covariate to show a clear trend with the magnitude of target earthquakes. Figure 11 plots the FLT values versus the magnitudes of the target earthquakes from 1951 to 2020. The locally weighted smoothed curve, shown by the solid black line, reveals an increasing trend with magnitude. This may not necessarily imply that future large earthquakes are more likely to occur on known faults than smaller earthquakes. It may instead reflect the fact that large earthquakes cause surface ruptures more frequently than small ones; consequently, new ruptures over the past 70 years have revealed the associated faults and allowed them to be mapped.

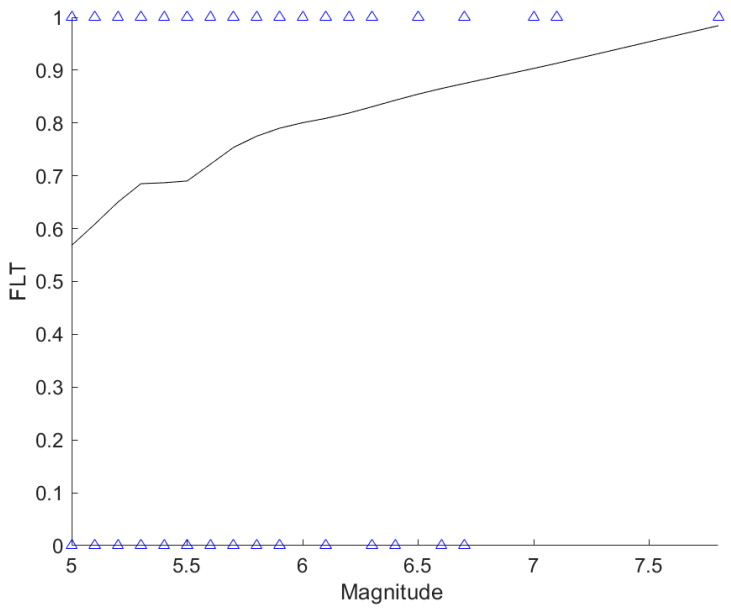


Figure 11. Fault covariate values for targeted earthquakes against magnitude, 1951–2020. The solid black line shows the smoothed scatter plot. The blue triangles depict the values of the FLT covariate for each target earthquake.

4. Discussion

The low information gain of hybrid models including strain rate covariates in reverse testing is consistent with the relatively low ASS values of the strain rate covariates and low strain rate values associated with target earthquakes from 1951 to 1986. The ASS values of the strain rate covariates in the reverse testing period are not only lower than in the fitting period but are also lower than the ASS values of the PPI and PMF covariates during the reverse testing period (Figures 7 and 8). The contrast of ASS values between the fitting and reverse testing periods is particularly strong for BSS. This explains the negative IGPEs for hybrids with BSS in the reverse testing period (Figure 3c).

Similarly, the large IGPE for hybrids with HWS in forward testing is consistent with the high ASS for HWS in 2012–2015 and with the slow tailing off between 2010 and 2020 of the trend in HWS associated with target earthquakes. Evidently, if the forward testing

period were extended through to 2020, hybrids including HWS would have continued to perform well.

Differences between the three present strain rate models can be attributed to the differences in the geodetic datasets on which they were based and the evolving techniques for estimating strain rates from the geodetic data. The most recently developed of the three models is the HWS model, which was published in 2020. HWS was derived from the most complete data and up-to-date techniques and showed the best correlation with the locations of the most recent earthquakes (Figure 7). However, all three strain rate models exhibit a disappointingly low correlation with the locations of earthquakes from 1951 to 1986.

The implicit assumption behind the fitting of hybrid models to estimate long-term earthquake rates is that the correlation between the covariates and the locations of target earthquakes is stable over time. Alternatively, if not stable over time, the correlation during the fitting period should be indicative of the long-term correlation. The correlations for PPI and PMF appear to be more stable over time than those for the strain rate covariates, based on the ASS variations. PPI and PMF represent features that are expected to affect earthquake occurrence over a long time frame. The greater instability of the correlation for strain rate covariates may be attributed to the short-term non-stationarity of earthquake occurrence. The strain rate covariates are most highly correlated with earthquake occurrence within the time period of the data on which they are based or within a few years after (Figure 7).

Without a dense GNSS network and extensive historical and paleo-seismicity records, it is not possible to pinpoint temporal and spatial variations of strain rates. Recently, Iezzi et al. obtained high temporal histories of slip rates for three parallel normal faults in central Greece with progressive clusters using in situ 36Cl cosmogenic dating [28]. They also had access to associated GNSS recordings of a dense network. They compared regional decadal geodetic strain rates with strain rates derived from slip-rate pulses over a few thousand years on each fault. They found that strain builds up across a fault system over thousands of years, but not all individual faults actively slip at the same time. They discussed how the available geodetic data alone was not capable of pinpointing the switchover of slip from one fault to another over time. In comparison, New Zealand has neither a dense GNSS network nor a comparable record of fault slip histories. The density of GNSS stations has been progressively improving but is still sparse in some parts and limited to onshore regions [14]. Obviously, this affects the accuracy of the strain rate models in NZ offshore regions, where many of the earthquakes occur.

Given the low earthquake location–strain rate correlations in the reverse testing period here, it is expected that there will be future periods during which such correlations are similarly low.

In fitting hybrid models for estimating long-term seismicity rates, it seems best to use the longest possible fitting period subject to earthquake catalogue quality considerations. The NZ catalogue covers about 180 years of historical and instrumental records. With the improvement of the NZ seismographic network, the magnitude of completeness has lowered to 5.0 for the recent 70 years of the GeoNet catalogue. Such a level of magnitude completeness fulfils the magnitude threshold of 4.95 applied to the target earthquakes for this study. However, we cannot be confident that a 70-year period, or any other fixed period, is long enough to represent the long-term spatial distribution of earthquakes. The main purpose of the hybrid fitting is to realistically weight the information offered by the available covariates, none of which depend directly on the catalogue. Here we showed that it would be unwise to base this weighting on a 20-year subset of the available catalogue. Performing tests with the 180-year catalogue could potentially help us to understand how adequate a 70-year catalogue is for fitting such hybrid models.

The robustness of our results against time-varying errors in earthquake locations could be questioned. However, since the strain rate models and all other covariates were defined on a rather coarse grid of 0.1×0.1-degree cells, they naturally can accommodate location errors without having much effect on the correlation with earthquake locations. We examined the robustness of the correlations between all covariates and target earthquake locations by

introducing synthetic location errors within the range reported by Bondár et al. [29] to be the most probable values for the ISC-GEM catalogue. The location errors were added to the epicentres of target events from 1987 onwards. We tested the hypothesis that events prior to 1987 had larger location errors due to the seismograph network's sparsity, and that could be the reason for low correlations between the covariates and target earthquake locations. However, this hypothesis was rejected; despite the added location errors for all the covariates, the main features of the smoothed curves were preserved.

5. Conclusions

We analysed the performance of multiplicative hybrid models in forward and reverse testing periods. To complement the performance analysis, we also obtained Molchan error diagrams and smoothed scatter plots of strain rate covariates versus time. All the analyses reveal strong variability over time in the correlation of strain rates with earthquake locations. These results suggest that strain rate models based on the available geodetic data for only a few decades may not be good indicators of where earthquakes occur over a long time frame. Therefore, the longest available high-quality earthquake catalogue should be used in constructing hybrid models to estimate long-term earthquake rates for seismic hazard analysis.

Author Contributions: Conceptualization, S.J.R., D.A.R. and M.C.G.; methodology, S.J.R. and D.A.R.; software, S.J.R., D.A.R. and C.R.; formal analysis, S.J.R. and D.A.R.; writing—original draft preparation, S.J.R. and D.A.R.; writing—review and editing, S.J.R., D.A.R., C.R. and M.C.G. All authors have read and agreed to the published version of the manuscript.

Funding: This research was funded by the Strategic Science Investment Fund (SSIF) and the National Seismic Hazard Model Revision Project of the Ministry of Business, Innovation and Employment of New Zealand.

Institutional Review Board Statement: Not applicable.

Informed Consent Statement: Not applicable.

Data Availability Statement: The New Zealand Earthquake Catalogue was obtained from GeoNet. Available online: http://www.geonet.org.nz (accessed on 30 May 2022). Data on earthquake faults and slip rates were obtained from the New Zealand Community Fault Model v1.0 (Data Set), GNS Science, https://doi.org/10.21420/NMSX-WP67 (accessed on 30 May 2022).

Acknowledgments: We acknowledge the New Zealand GeoNet project and its sponsors EQC, GNS Science, LINZ, NEMA, and MBIE for providing the data used in this study. Kiran Kumar Thingbaijam and David Burbidge provided helpful internal reviews of the manuscript.

Conflicts of Interest: The authors declare no conflict of interest. The funders had no role in the design of the study; in the collection, analyses, or interpretation of data; in the writing of the manuscript, or in the decision to publish the results.

Appendix A

Appendix A.1 Strain Rate Covariates

Beavan and Haines [30] utilized GNSS data from 9 geodetic networks across NZ, comprising 362 GNSS stations. They calculated continuous horizontal velocity and associated strain rate fields at the Earth's surface in NZ between 1991 and 1998. They adopted the method proposed by Haines et al. [26], which enhanced NZ's known deformations and discovered new features in both the North and South Islands.

John Beavan (1950–2012) directed most of the GNSS data acquisition in NZ [14]. His last shear strain rate model of NZ was based on survey-mode GNSS data collected in NZ between January 1996 and February 2011. This model was based on the method of Beavan and Haines [30] and was submitted to Land Information New Zealand (LINZ) to be used in updating the geodetic and cadastral systems following the 4 September 2010 Darfield earthquake. This was the shear strain rate (BSS) used by Rhoades et al. [11].

The Global Strain Rate Model (GSRM v.2.1) of Kreemer et al. [13] is an improved version of the GSRM-1 Kreemer et al. model in [2] with a larger input dataset and improved spatial resolution. The maximum shear strain rate from GSRM v.2.1 is referred to here as the GSS model. Like the BSS model, the GSS model was obtained using the Haines and Holt method [25,27,30] to model the strain rate field. GSS is derived from worldwide GNSS data between 1 January 1996 and 31 December 2013, including velocities from 233 published and unpublished regionally focused studies. Table A1 lists the NZ-focused studies used in the GNSS compilation of the GSS model [13]. Apart from in the southeast South Island region, the GSS model uses less up-to-date data than the BSS model.

The NZ strain rate model of Haines and Wallace [14] was produced from GNSS interseismic velocities at 918 stations between 1995 and 2013 [31]. This model was based on the novel method of Haines et al. [32]. They used a physics-based approach to invert the GNSS displacement fields for Vertical Derivatives of Horizontal Stress (VDoHS) rates. This method uses constraints from linear elasticity in place of artificial smoothing. This is to ensure physical plausibility, higher resolution, and an improved signal-to-noise ratio compared to the commonly used methods of Haines and Holt [25] and Beavan and Haines [30]. The one modification made to the published Haines and Wallace model of [14] is one implemented by the NSHM Geodesy Working Group: a sill model of rapid magmatic contraction in the Taupo Volcanic Zone (TVZ) was removed from the GNSS velocities, and then the velocities were re-inverted using the Haines et al. [32] method [31]. The maximum shear strain rate from this modified model is the scalar quantity that we use in our hybrid modelling and is henceforth referred to as HWS [33].

Table A1. Data from NZ GNSS campaigns used in constructing the GSS rate model.

Reference	Region
Beavan et al. (1999) [34]	Central Southern Alps, NZ, Alpine Fault
Beavan and Haines (2001) [30]	NZ
Darby and Beavan (2001) [35]	Southernmost North Island, NZ
Denys et al. (2014) [36]	Southeast South Island, NZ

Appendix B

Appendix B.1 Proximity to the Plate Interface (PPI)

A PPI covariate was initially introduced by Rhoades et al. [10]. Here we use a modified version of PPI that differs in some minor details ([33]; Figure 1a). PPI is based on the notion of proximity to the plate interface. A map of the interface between the Australian and Pacific plates in the Hikurangi subduction zone [37] is used to define the North Island plate boundary. South of the Hikurangi subduction zone, the plate boundary is defined by the Hope Fault, the Alpine Fault, and the Fiordland subduction interface, as given in the 2010 NZNSHM fault model [38]. In estimating the proximity of a cell to the interface, no allowance is made for the possibility of different slip rates on different patches of the plate boundary. The plate boundary is represented by a set of n_I points on the interface at approximately 1 km spacing, and a cell is represented by a set of n_c points at its middle latitude and longitude coordinates with depths from 1 to 39 km at a spacing of 2 km. The PPI covariate $\rho(j)$ in the jth grid cell is defined by

$$\rho(j) = \frac{1}{n_c} \sum_{l=1}^{n_c} h(j,l), \tag{A1a}$$

where $h(i,l)$ is an index of the proximity of the lth point in the jth cell to ith point on the interface:

$$h(j,l) = \frac{1}{\left[d_I^2 + \min(\Delta(i,l)^2)_{i=1,\ldots,n_I}\right]^{3/2}}, \tag{A1b}$$

where $\Delta(i,l)$ is the distance in km from $[x_I(i), y_I(i), z_I(i)]$ to $[x_j(l), y_j(l), z_j(l)]$ and d_I is a constant smoothing distance, taken as 10 km.

Appendix B.2 Proximity to Mapped Faults (PMF)

The concept of proximity to mapped faults was initially introduced by Rhoades and Stirling [39]. It takes account of the distance from the jth cell to all fault elements and their associated slip rates, assumed uniform on each fault segment. As in [39], each fault plane is divided into numerous point sources closely spaced at intervals of 1 km. Thus the set of fault segment planes and associated slip rates is expanded into a much larger set of point sources, at longitude, latitude, and depth coordinates $[x_F(i), y_F(i), z_F(i)]$, $i = 1, \cdots, n_F$, and with associated slip rates $r_i, i = 1, \cdots, n_F$. Similarly, a cell with dimensions of 0.1 degrees in latitude and longitude and 40 km in depth is expanded into a representative set of points within it $[x_j(l), y_j(l), z_j(l)]$, $l = 1, \cdots, n_c$ on a cuboidal grid spaced at 0.033 degrees in latitude and longitude and 5 km in depth. Following [10], the PMF covariate $\rho(j)$ in the jth grid cell is defined by

$$\rho(j) = \frac{1}{n_c n_f} \sum_{i=1}^{n_f} \sum_{l=1}^{n_c} h(i,l), \tag{A2}$$

where $h(i,l)$ is an index of the proximity of the lth point in the jth cell to slip on the ith fault point source:

$$h(i,l) = \frac{r_i}{\left[d_F^2 + \Delta(i,l)^2\right]^{\frac{3}{2}}}, \tag{A3}$$

where r_i is the slip rate in mm/yr, $\Delta(i,l)$ is the distance in km from $[x_F(i), y_F(i), z_F(i)]$ to $[x_j(l), y_j(l), z_j(l)]$, and d_F is a constant smoothing distance. The value of $\rho(j)$ is, therefore, high for cells near to, or intersected by, mapped faults and low far away from mapped faults. Further, $\rho(j)$ is greater when the slip rates of nearby mapped faults are greater.

Here we used a modified version [33]. In the modified PMF fault, sources are planes rather than linear traces and distances are measured in three dimensions rather than two. Rhoades and Stirling [39] found an optimal smoothing distance of 1.0 km for a PMF model defined in continuous space. Rhoades et al. used a smoothing distance of 2.5 km, but their PMF has since been found to have small-scale variations between adjacent cells due to the smoothing distance being too small [10]. Here we use a larger smoothing distance of $d_F = 10$ km, so that the denominators in Equation (5) are not overly sensitive to the exact positions of points on the fault surfaces and within the cells. The PMF covariate used here (Figure 1b) also uses updated fault information from the New Zealand Community Fault Model [18].

Appendix B.3 Fault in Cell (FLT)

The fault in cell (FLT) covariate [10] is defined to have the value 1 if a fault intersects the cell anywhere between the surface and a depth of 40 km, given the surface trace of the fault, its dip angle and estimated width. Otherwise, it takes the value 0. The FLT covariate is shown in Figure 1c [33] and has been updated using all faults from the New Zealand Community Fault Model [18].

References

1. Ward, S.N. On the consistency of earthquake moment rates, geological fault data, and space geodetic strain: The United States. *Geophys. J. Int.* **1998**, *134*, 172–186. [CrossRef]
2. Kreemer, C.; Holt, W.E.; Haines, A.J. The global moment rate distribution within plate boundary zones. In *Plate Boundary Zones*; Stein, S., Freymueller, J.T., Eds.; AGU: Washington, DC, USA, 2002; pp. 173–190.
3. Bird, P.; Kreemer, C.; Holt, W.E. A Long-term Forecast of Shallow Seismicity Based on the Global Strain Rate Map. *Seismol. Res. Lett.* **2010**, *81*, 184–194. [CrossRef]
4. Bird, P.; Jackson, D.D.; Kagan, Y.Y.; Kreemer, C.; Stein, R.S. GEAR1: A Global Earthquake Activity Rate Model Constructed from Geodetic Strain Rates and Smoothed Seismicity. *Bull. Seismol. Soc. Am.* **2015**, *105*, 2538–2554. [CrossRef]

5. Mazzotti, S.; Leonard, L.J.; Cassidy, J.F.; Rogers, G.C.; Halchuk, S. Seismic hazard in western Canada from GPS strain rates versus earthquake catalog. *J. Geophys. Res. Earth Surf.* **2011**, *116*, B12310. [CrossRef]
6. Rhoades, D.A.; Gerstenberger, M.C.; Christophersen, A.; Zechar, J.D.; Schorlemmer, D.; Werner, M.; Jordan, T.H. Regional Earthquake Likelihood Models II: Information Gains of Multiplicative Hybrids. *Bull. Seismol. Soc. Am.* **2014**, *104*, 3072–3083. [CrossRef]
7. Field, E.H. Overview of the Working Group for the Development of Regional Earthquake Likelihood Models (RELM). *Seismol. Res. Lett.* **2007**, *78*, 7–16. [CrossRef]
8. Schorlemmer, D.; Gerstenberger, M.C. RELM Testing Center. *Seismol. Res. Lett.* **2007**, *78*, 30–36. [CrossRef]
9. Zechar, J.D.; Schorlemmer, D.; Werner, M.; Gerstenberger, M.C.; Rhoades, D.; Jordan, T.H. Regional Earthquake Likelihood Models I: First-Order Results. *Bull. Seismol. Soc. Am.* **2013**, *103*, 787–798. [CrossRef]
10. Rhoades, D.A.; Christophersen, A.; Gerstenberger, M.C. Multiplicative Earthquake Likelihood Models Based on Fault and Earthquake Data. *Bull. Seismol. Soc. Am.* **2015**, *105*, 2955–2968. [CrossRef]
11. Rhoades, D.; Christophersen, A.; Gerstenberger, M. Multiplicative earthquake likelihood models incorporating strain rates. *Geophys. J. Int.* **2017**, *208*, 1764–1774. [CrossRef]
12. Beavan, J.; Wallace, L.M.; Palmer, N.; Denys, P.; Ellis, S.; Fournier, N.; Hreinsdottir, S.; Pearson, C.; Denham, M. New Zealand GPS velocity field: 1995–2013. *N. Z. J. Geol. Geophys.* **2016**, *59*, 5–14. [CrossRef]
13. Kreemer, C.; Blewitt, G.; Klein, E.C. A geodetic plate motion and Global Strain Rate Model. *Geochem. Geophys. Geosyst.* **2014**, *15*, 3849–3889. [CrossRef]
14. Haines, A.J.; Wallace, L.M. New Zealand-Wide Geodetic Strain Rates Using a Physics-Based Approach. *Geophys. Res. Lett.* **2020**, *47*, e2019GL084606. [CrossRef]
15. Rhoades, D.A.; Schorlemmer, D.; Gerstenberger, M.C.; Christophersen, A.; Zechar, J.D.; Imoto, M. Efficient testing of earthquake forecasting models. *Acta Geophys.* **2011**, *59*, 728–747. [CrossRef]
16. Hurvich, C.M.; Tsai, C.-L. Regression and time series model selection in small samples. *Biometrika* **1989**, *76*, 297–307. [CrossRef]
17. Gerstenberger, M.C.; Rhoades, D.A. New Zealand Earthquake Forecast Testing Centre. *Pure Appl. Geophys.* **2010**, *167*, 877–892. [CrossRef]
18. Van Dissen, R.; Seebeck, H.; Litchfield, N.; Barnes, P.; Nicol, A.; Langridge, R.; Barrell, D.; Villamor, P.; Ellis, S.; Rattenbury, M.; et al. Development of the New Zealand Community Fault Model version 1.0. In Proceedings of the NZSEE Annual Technical Conference, Christchurch, New Zealand, 15 April 2021; p. 92.
19. Molchan, G. Strategies in strong earthquake prediction. *Phys. Earth Planet. Inter.* **1990**, *61*, 84–98. [CrossRef]
20. Molchan, G.M. Structure of optimal strategies in earthquake prediction. *Tectonophysics* **1991**, *193*, 267–276. [CrossRef]
21. Green, D.M.; Swets, J.A. *Signal Detection Theory and Psychophysics*; John Wiley: Oxford, UK, 1966.
22. Fawcett, T. An introduction to ROC analysis. *Pattern Recognit. Lett.* **2006**, *27*, 861–874. [CrossRef]
23. Zechar, J.D.; Jordan, T.H. The Area Skill Score Statistic for Evaluating Earthquake Predictability Experiments. *Pure Appl. Geophys.* **2010**, *167*, 893–906. [CrossRef]
24. Cleveland, W.S. Robust Locally Weighted Regression and Smoothing Scatterplots. *J. Am. Stat. Assoc.* **1979**, *74*, 829–836. [CrossRef]
25. Haines, A.J.; Holt, W.E. A procedure for obtaining the complete horizontal motions within zones of distributed deformation from the inversion of strain rate data. *J. Geophys. Res. Earth Surf.* **1993**, *98*, 12057–12082. [CrossRef]
26. Haines, A.J.; Jackson, J.A.; Holt, W.E.; Agnew, D.C. *Representing Distributed Deformation by Continuous Velocity Fields*; Sci. Rep.98/5; GNS Science: Lower Hutt, New Zealand, 1998; p. 110.
27. Holt, W.E.; Shen-Tu, B.; Haines, J.; Jackson, J. On the determination of self-consistent strain rate fields within zones of distributed continental deformation. *Geophys. Monogr. Ser.* **2000**, *121*, 113–141. [CrossRef]
28. Iezzi, F.; Roberts, G.; Walker, J.F.; Papanikolaou, I.; Ganas, A.; Deligiannakis, G.; Beck, J.; Wolfers, S.; Gheorghiu, D. Temporal and spatial earthquake clustering revealed through comparison of millennial strain-rates from 36Cl cosmogenic exposure dating and decadal GPS strain-rate. *Sci. Rep.* **2021**, *11*, 23320. [CrossRef] [PubMed]
29. Bondár, I.; Engdahl, E.R.; Villaseñor, A.; Harris, J.; Storchak, D. ISC-GEM: Global instrumental earthquake catalogue (1900–2009), II. Location and seismicity patterns. *Phys. Earth Planet. Inter.* **2015**, *239*, 2–13. [CrossRef]
30. Beavan, J.; Haines, J. Contemporary horizontal velocity and strain rate fields of the Pacific-Australian plate boundary zone through New Zealand. *J. Geophys. Res. Earth Surf.* **2001**, *106*, 741–770. [CrossRef]
31. Johnson, K.; Wallace, L.M.; Maurer, J.; Hamling, I.; Williams, C.; Rollins, C.; Gerstenberger, M. The 2022 New Zealand National Seismic Hazard Model: Geodetic Deformation Model, GNS Science Report. In Proceedings of the 2021 New Zealand Society for Earthquake Engineering Annual Technical Conference, Christchurch, New Zealand, 15 April 2021.
32. Haines, A.J.; Dimitrova, L.L.; Wallace, L.M.; Williams, C.A. Enhanced Surface Imaging of Crustal Deformation: Obtaining Tectonic Force Fields Using GPS Data. Springer Briefs in Earth Sciences. 2015. 99p. Available online: https://link.springer.com/book/10.1007/978-3-319-21578-5 (accessed on 1 April 2022).
33. Rastin, S.J.; Rhoades, D.A.; Rollins, C.; Gerstenberger, M.C.; Christophersen, A. *Spatial Distribution of Earthquake Occurrence for the New Zealand National Seismic Hazard Model Revision*; GNS Science report, SR 2021/51; GNS Science: Lower Hutt, New Zealand, 2022. [CrossRef]

34. Beavan, J.; Moore, M.; Pearson, C.; Henderson, M.; Parsons, B.; Bourne, S.; England, P.; Walcott, D.; Blick, G.; Darby, D.; et al. Crustal deformation during 1994–1998 due to oblique continental collision in the central Southern Alps, New Zealand, and implications for seismic potential of the Alpine fault. *J. Geophys. Res. Earth Surf.* **1999**, *104*, 25233–25255. [CrossRef]
35. Darby, D.; Beavan, J. Evidence from GPS measurements for contemporary interplate coupling on the southern Hikurangi subduction thrust and for partitioning of strain in the upper plate. *J. Geophys. Res. Earth Surf.* **2001**, *106*, 30881–30891. [CrossRef]
36. Denys, P.; Norris, R.; Pearson, C.; Denham, M. A Geodetic Study of the Otago Fault System of the South Island of New Zealand. In *Earth on the Edge: Science for a Sustainable Planet*; Rizos, C., Willis, P., Eds.; International Association of Geodesy Symposia; Springer: Berlin/Heidelberg, Germany, 2014; Volume 139. [CrossRef]
37. Williams, C.A.; Eberhart-Phillips, D.; Bannister, S.; Barker, D.H.N.; Henrys, S.; Reyners, M.; Sutherland, R. Revised Interface Geometry for the Hikurangi Subduction Zone, New Zealand. *Seismol. Res. Lett.* **2013**, *84*, 1066–1073. [CrossRef]
38. Stirling, M.; McVerry, G.; Gerstenberger, M.; Litchfield, N.; Van Dissen, R.; Berryman, K.; Barnes, P.; Wallace, L.; Villamor, P.; Langridge, R.; et al. National Seismic Hazard Model for New Zealand: 2010 Update. *Bull. Seismol. Soc. Am.* **2012**, *102*, 1514–1542. [CrossRef]
39. Rhoades, D.A.; Stirling, M.W. An Earthquake Likelihood Model Based on Proximity to Mapped Faults and Cataloged Earthquakes. *Bull. Seismol. Soc. Am.* **2012**, *102*, 1593–1599. [CrossRef]